

Design and implementation of reconfigurable MIMO antennas for radar applications

Faisal Alwatban, Nawaf Almushaiti, Khaled Almoshaiti, Abdulaziz Alnogithan, Abdulelah Als Salman, Azzam Alhumaid, Mahmoud Shaban

This work presents the design and development of a high-performance frequency-reconfigurable multiple-input multiple-output (MIMO) antenna for the 24 GHz Industrial, Scientific, and Medical (ISM) band, targeting advanced sensing and automotive radar systems. The proposed antenna utilizing a varactor diode to enable agile frequency tuning across a 500 MHz bandwidth (23.8-24.3 GHz), ensuring adaptability to dynamic spectral requirements. The design incorporates four-port MIMO configurations, each integrating a 1×8 microstrip patch array with an optimized split-ring resonator metamaterial absorber. This engineered absorber assessed in suppressing mutual coupling by disrupting surface wave propagation, achieving exceptional inter-port isolation of 38.4 dB and a peak gain of 17.8 dBi at the resonance frequency of 24.12 GHz. Key radiation characteristics include an E-plane beamwidth of 74° and H-plane beamwidth of 11°, coupled with a side-lobe level (SLL) suppressed to -21 dB, ensuring precise directional control and minimal off-axis interference. With an envelope correlation coefficient (ECC) below 0.0004, the antenna demonstrates robust performance in spectral efficiency, diversity gain, and channel capacity. These attributes position the design as a promising solution for high-density wireless environments, offering reconfigurability feature, interference mitigation, and high gain for next-generation of mmWave sensing applications.

Keywords: antennas, MIMO systems, radar systems, 5G mmWave, sidelobe level, mutual coupling

1 Introduction

Contemporary automotive systems increasingly integrate advanced technologies such as adaptive cruise control, pedestrian detection, and collision avoidance, driven by the rising demand for autonomous driving. This evolution has propelled the need for highly reliable millimeter-wave (mmWave) radar sensors, particularly within the 24 GHz, 77 GHz, and 79 GHz frequency bands [1-5]. Tailored for short-range operations, the 24 GHz band supports blind-spot monitoring and medical applications like heart rate detection via compact, high-frequency antennas compatible with RF system-on-chip designs. In contrast, the 77 GHz band enables long-range functionalities, such as adaptive cruise control, while the 79 GHz band offers high-resolution short-range detection. Despite its utility, the Industrial, Scientific, and Medical (ISM) band comprising the ISM-24GHz band faces challenges like mutual coupling between transceiver antennas, which can compromise sensor performance. Mitigation strategies, including advanced decoupling techniques, are critical to enhancing reliability in healthcare and automotive applications [6-13].

mmWave radars, operating in the frequency range of 24 GHz to 100 GHz, have become increasingly important in both civil and defence sectors due to their high resolution, compact form factor, and ability to operate effectively in various environmental conditions. In civil applications, mmWave radars are widely used in auto-

motive systems for advanced driver-assistance systems (ADAS), enabling features such as collision avoidance, blind-spot detection, and adaptive cruise control. They are also utilized in healthcare for non-invasive monitoring, in industrial automation for precision sensing, and in 5G networks for high-speed data transmission. In the defence sector, mmWave radars are critical for surveillance, target detection, and tracking, offering high-resolution imaging and the ability to penetrate adverse weather conditions, which is essential for mission-critical operations. However, the deployment of mmWave radars faces several challenges. These include high atmospheric attenuation, limited range due to signal absorption by rain and humidity, and susceptibility to interference from other mmWave devices. Additionally, designing compact, cost-effective, and energy-efficient systems with low side-lobe levels (SLL) and high isolation remains a significant technical hurdle. Addressing these challenges requires advancements in materials, antenna design, signal processing, and integration techniques. Despite these obstacles, the unique capabilities of mmWave radars make them indispensable for modern applications, driving ongoing research and innovation in this field.

Anticipated advancements in radar technology may extend to higher mmWave (100-300 GHz) and sub-terahertz (100-1000 GHz) bands, addressing ultra-high-resolution demands for next-generation systems [14-16]. Concurrently, Multiple-Input Multiple-Output (MIMO) technology has emerged as a transformative approach,

utilizing spatial diversity to enhance radar communications. MIMO configuration, in wireless systems, improves throughput and data link stability through multipath exploitation, while in radar, it enables superior target resolution and robustness against interference. Virtual array techniques further amplify these benefits by synthesizing larger apertures from smaller physical arrays, circumventing spatial and cost constraints while boosting angular coverage and sensitivity [17].

A critical focus in MIMO radar design is side lobe suppression, which minimizes spurious detections and enhances target discrimination in complex environments. Recent innovations in reconfigurable MIMO antennas for 24 GHz applications underscore progress in mmWave systems. These antennas adapt dynamically via frequency, polarization, or radiation pattern adjustments, optimizing performance across wireless, IoT, and radar domains. PIN and varactor diodes are commonly employed for reconfigurability, though their trade-offs, such as limited tuning ranges and nonlinear responses, necessitate careful design [18-20].

Reference [18] introduces a lens-based reconfigurable MIMO architecture for mmWave communications, addressing path loss and channel sparsity through multi-pattern radiation. Building on this, [19] explores metamaterial-enhanced MIMO designs to mitigate mutual coupling, vital for 5G and beyond. Meanwhile, [20] analyses planar MIMO antennas, emphasizing spatial diversity to overcome mmWave limitations like surface waves. In marine contexts, [21] adapts 24 GHz FMCW MIMO radar for target tracking, demonstrating efficacy through simulations and field trials. Additionally, [22] achieves a -28 dB side lobe level in a compact 24 GHz comb array, while [23] utilizes reconfigurable intelligent surfaces (RIS) to optimize channel characteristics in massive MIMO systems.

This work presents a series-fed reconfigurable 4-port MIMO array for 24 GHz radar, demonstrating enhanced gain, isolation, and side lobe suppression through meticulous design and simulation. The findings highlight significant improvements in mutual coupling reduction and reconfigurability, advancing the state-of-the-art in compact, high-performance radar systems.

2 Materials and methods

2.1 Design of single-element antenna array

Microstrip antennas, often termed patch antennas, consist of a thin metallic patch ($t \ll \lambda_0$) positioned on a dielectric substrate above a ground plane, with a height which is typically between $0.003 \lambda_0$ and $0.05 \lambda_0$. This compact design ($h \ll \lambda_0$) makes them significantly smaller than the operating wavelength. The substrate is usually photolithographically etched to form radiating elements and feed lines. These antennas support diverse

patch geometries – rectangular, circular, dipole-like strips, elliptical, square or triangular – offering flexibility in design [24].

Renowned for their compactness and intrinsic wide bandwidth, microstrip antennas are ideal for array configurations. They can produce both linear and circular polarizations, enhancing their adaptability across applications. The rectangular patch is the most prevalent design due to its simplicity and compatibility with analytical models like the transmission-line and cavity models. The transmission-line model, favoured for its straightforward application, efficiently analyses rectangular patches and is particularly suited for thin substrates. In this model, the antenna is represented as two radiating slots separated by a low-impedance transmission line (characteristic impedance, Z_0), with dimensions $W_p \times L_p \times h$, where W_p , L_p , and h denote patch width, length, and substrate thickness, respectively. Field fringing occurs at the patch edges due to its finite size, extending the effective electrical length. The extent of fringing depends on patch dimensions, substrate height, and dielectric constant. Although designs with $L_p/h > 1$ reduce fringing, residual effects still shift the resonant frequency f_r , necessitating careful calibration during design [24].

In this study, the antenna is engineered to operate at a resonant frequency $f_r = 24.125$ GHz, corresponding to the ISM band, with a targeted bandwidth exceeding 500 MHz. A critical design consideration involves balancing substrate thickness against performance metrics: increasing h enhances bandwidth but reduces radiation efficiency due to heightened surface wave losses and substrate-induced dispersion.

Once the width and length of a single microstrip patch have been determined, designing an array of such elements enhances gain but introduces undesirable side lobes in the radiation pattern [24]. The array factor (AF) of an antenna array describes how the combined signal from an array of antennas varies with direction, and it is given by

$$AF(\theta) = \sum_{k=1}^N w_n e^{j(n-1)kd \cos(\theta)} \quad (1)$$

where angle θ represents the direction in which the antenna array's radiation pattern is being evaluated. The equation indicates that the contributions from all N elements in the antenna array are being summed. The term w_n represents the weighting factor or complex excitation coefficient for the n th element in the array. This weighting factor determines both the amplitude and phase of the signal fed to or received from each antenna element. By adjusting these weights, the radiation pattern of the array can be shaped or steered in a desired direction, enabling functionalities like beamforming or null steering. The exponential term $e^{j(n-1)kd \cos(\theta)}$

accounts for the phase differences between the signals from different antenna elements. k is the wave number, typically defined as $2\pi/\lambda$, where λ is the wavelength of the signal. d is the spacing between adjacent antenna elements in the array. The term $kd \cos(\theta)$ represents the phase shift caused by the physical separation d between the antenna elements.

In this regard, manipulating the weights and spacing, specific directional properties of the designed antenna such as focusing energy in a particular direction or suppressing interference from unwanted directions can be attained. The design process for a microstrip patch array begins with determining the dimensions of a single patch, including its width and length. Once these parameters are established, an array of such elements is designed to enhance gain. However, this approach introduces undesirable side lobes in the radiation pattern, which can degrade performance. To address this issue, the Dolph-Chebyshev method is employed, offering a systematic approach to suppress side lobes while maintaining high directivity. This method leverages Chebyshev polynomials, known for their equiripple property, to optimize the excitation coefficients of the array elements and achieve a predefined side-lobe level (SLL).

To suppress these side lobes while maintaining high directivity, the Dolph-Chebyshev method offers a systematic approach. This technique utilizes Chebyshev polynomials, known for their equiripple property, to achieve a predefined SLL by optimizing the excitation coefficients of the array elements. The process begins by defining critical parameters such as the number of elements (N), the desired SLL (e.g., -25 dB), and the element spacing (d), which is typically set to $(\lambda/2)$ to suppress effect of grating lobes. The order (m) of Chebyshev polynomial ($T_m(x)$) is selected based on the array size, where $(m = N - 1)$.

$$T_m(x) = \begin{cases} \cos(m \cos^{-1}(x)) & \text{if } |x| \leq 1 \\ \cosh(m \cosh^{-1}(x)) & \text{if } |x| > 1 \end{cases} \quad (2)$$

This can be expressed as a polynomial form as follows:

$$T_0(x) = 1, \quad T_1(x) = x$$

$$T_{m+1}(x) = 2xT_m(x) - T_{m-1}(x) \quad \text{for } m \geq 1 \quad (3)$$

The polynomial's argument x is scaled to align the AF visible region with the equiripple region of the polynomial. Therefore, a scaling parameter x_0 related to the desired SLL is calculated using [25]:

$$x_0 = \cosh\left(\frac{\cosh^{-1}\left(10^{\frac{SLL}{20}}\right)}{(N-1)}\right) \quad (4)$$

The array factor (AF) of an antenna array is then recomputed as:

$$\begin{aligned} AF(\theta) &= \sum_{k=1}^N w_n e^{j(n-1)kd \cos(\theta)} \\ &= T_{N-1}\left(x_0 \cos\left(\frac{\pi d \cos(\theta)}{\lambda}\right)\right) \end{aligned} \quad (5)$$

The excitation coefficients w_n for each element are computed by expanding $T_m(x)$ and solving for the relative current amplitudes. These coefficients often follow a symmetric taper, simplifying the design of the feed network. The synthesized array factor is combined with the radiation pattern of the individual microstrip patch to generate the total radiation pattern.

In practice, implementing this method involves balancing trade-offs. Lowering the SLL increases the main-lobe beamwidth and the dynamic range of excitation currents, which can complicate the design of the feed network. Additionally, mutual coupling between patches and substrate effects must be considered, often requiring iterative tuning using electromagnetic simulation tools. For example, an 8-element array targeting a -25 dB SLL would employ the Chebyshev polynomial $T_7(x)$, with x_0 adjusted to constrain side-lobe peaks to the specified level. The resulting excitation coefficients taper symmetrically from the array's center, ensuring optimal performance. While the Dolph-Chebyshev method provides precise control over SLL and directivity, extreme current ratios between elements may pose challenges in practical implementation. Nonetheless, its analytical rigor and adaptability to linear, planar, or conformal arrays make it indispensable for applications like radar, satellite communications, and 5G systems, where interference suppression and directional accuracy are critical. The excitation coefficients for each element are computed by expanding $T_m(x)$ and equating terms to solve for the relative current amplitudes w_n .

$$\begin{aligned} w_n &= T_{N-1}\left(x_0 \cos\left(\frac{(2n-1)\pi}{2N}\right)\right) \\ &= T_7\left(x_0 \cos\left(\frac{(2n-1)\pi}{2N}\right)\right) \end{aligned} \quad (6)$$

Finally, the normalized polynomial coefficients (weights) derived from this methodology can be expressed as

$$[0.37783486, 0.58427224, 0.8424153, 1.0, 1.0, 0.8424153, 0.58427224, 0.37783486]$$

The prescribed amplitude distribution in Dolph-Chebyshev AF for the antenna employs normalized excitation weights spanning approximately 0.38 to 1.0, reflecting a systematic amplitude tapering to achieve optimized radiation characteristics. The central element, assigned the maximum amplitude coefficient (1.0), functions as the principal radiator, dictating the main lobe's directionality and gain. Adjacent elements exhibit

progressively reduced amplitudes (e.g., ~ 0.84), strategically reinforcing the main beam's constructive interference while suppressing grating lobes. Peripheral elements, with minimized weights (~ 0.38), are tailored to attenuate SLL by balancing destructive interference patterns. This symmetric amplitude profile – centrosymmetric about the primary radiator – embodies the Dolph-Chebyshev synthesis methodology, which enforces an equiripple sidelobe distribution to meet predefined SLL specifications. The design ensures a focused radiation pattern with enhanced directivity and controlled sidelobe degradation, critical for applications demanding spatial selectivity and interference mitigation. Such a configuration exemplifies the interplay between amplitude tapering and radiation efficiency, where judicious weight allocation optimizes the trade-off between beamwidth and sidelobe suppression.

2.2 Evaluation metrics of MIMO antenna

Typically, MIMO antennas are assessed by means of critical performance metrics to evaluate their effectiveness in wireless communication. These metrics including: Envelope Correlation Coefficient (ECC) that measures similarities of signal envelopes received by dissimilar antennas. Lower ECC values indicate reduced correlation and improved spatial diversity. Diversity Gain (DG) quantifies the improvement in signal reliability by leveraging multiple antennas to combat fading. Mean Effective Gain (MEG) evaluates the average power received by an antenna across all directions. Effective Diversity Gain (EDG) combines DG and ECC effects to reflect real-world performance. Lastly, Channel Capacity Loss (CCL) quantifies data rate degradation due to channel imperfections. Together, these metrics ensure robust MIMO system design for

applications like 5G and IoT, balancing theoretical ideals with practical challenges such as interference and noise.

3 Results and discussion

3.1 Single-array antenna

The designs proposed here employ a Rogers RT/Duroid 5880 substrate with $h=0.787$ mm, permittivity ϵ_r of 2.2, and loss tangent of 0.0009. Selection of the appropriate substrate fundamentally governs the antenna's performance by balancing impedance matching, radiation characteristics, and antenna efficiency. Figure 1 depicts optimized geometry of the series-fed 8-element array, with critical dimensions (e.g., microstrip feedlines, patch length W_p and width L_p) detailed in Tab. 1. The design leverages the Dolph-Chebyshev synthesis method to achieve precise amplitude tapering, assigning normalized current ratios of $I_1 : I_2 : I_3 : I_4 = 1 : 0.84 : 0.68 : 0.37$ across adjacent patches. These ratios translate to scaled patch widths of $W_{p1} : W_{p2} : W_{p3} : W_{p4} = 1 W_{p1} : 0.84 W_{p1} : 0.68 W_{p1} : 0.34 W_{p1}$ ensuring controlled radiation intensity and sidelobe suppression. A uniform inter-patch separation distance L_f and patch length W_p are maintained to preserve phase coherence. The antenna array is terminated with a varactor diode (VD) connected to an auxiliary patch $W_{pp} \times L_{pp}$, enabling tunable performance. Impedance matching is achieved via a microstrip feedline (width W_m , length L_m) connected to an SMA RF connector (dimensions L_{mf} and W_{mf}), ensuring minimal reflection losses and efficient signal transmission. This systematic integration of substrate properties, amplitude-weighted patches, and feedline optimization results in a high-performance array tailored for precise beamforming and operational robustness.

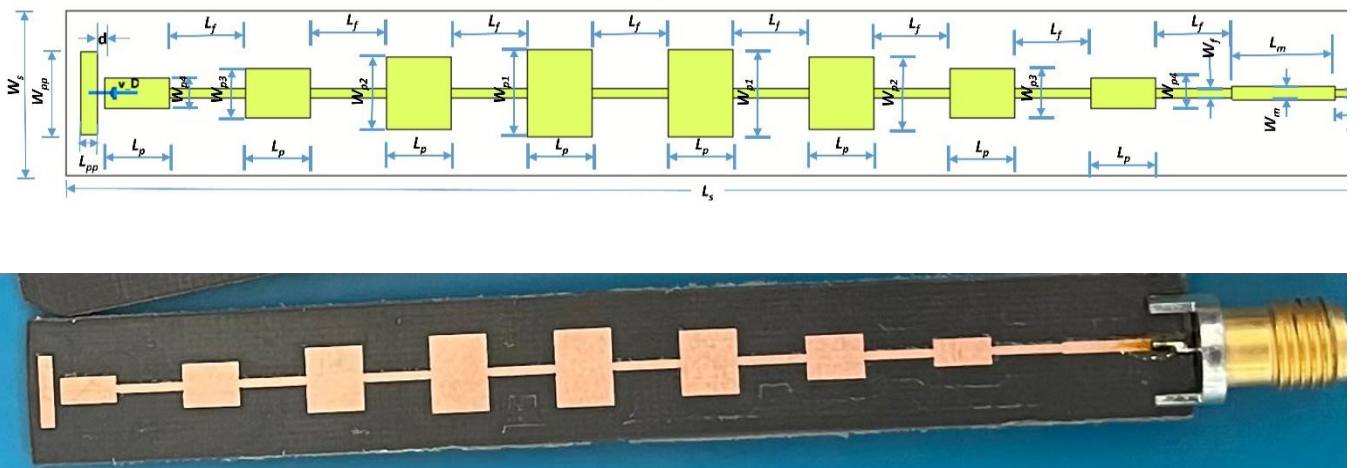


Fig. 1. Proposed design of antenna array: (top) geometry and dimensions, and (bottom) fabricated prototype

Table 1. Dimensions of the proposed design of antenna array

Parameter	W_{p1}	W_{p2}	W_{p3}	W_{p4}	L_p	W_s	L_s	W_{mf}	L_{mf}	W_m	L_m	W_f	L_f	W_{pp}	L_{pp}	d	W_g	L_g
Value (mm)	5.31	4.46	3.03	1.86	3.96	10	80	0.48	2.37	0.81	6.30	0.59	4.66	5.00	1.00	0.50	10.0	80.0

Figure 2(a) demonstrates the simulated reflection coefficient ($|S_{11}|$) of the antenna array, validating its precise resonance at 24.1 GHz with a minimal reflection magnitude of -38 dB, indicative of robust impedance matching. The operational bandwidth spans 23.85–24.23 GHz, achieving a 380 MHz bandwidth (-10 dB criterion) centered at the target frequency. Figure 2(b) further corroborates this performance by plotting the input impedance components (real Z_{real} and imaginary Z_{imag}) across the frequency spectrum. At resonance 24.1 GHz,

Z_{real} aligns closely with the system's characteristic impedance 50Ω , while Z_{imag} intersects zero, confirming the elimination of reactive components. This behavior underscores optimal power transfer efficiency, ensuring minimal signal reflection and maximal energy radiation at the operating frequency. Together, these results affirm the antenna array's suitability for high-frequency applications requiring precise frequency alignment and reliable impedance matching.

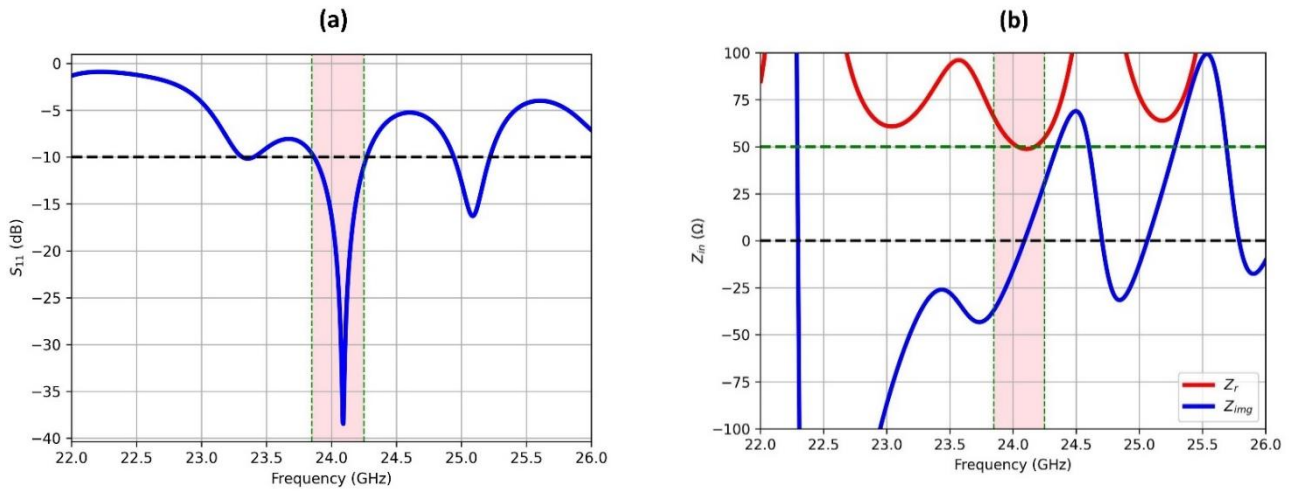


Fig. 2. (a) Reflection coefficient of the antenna array, and (b) the real and imaginary components of the input impedance at the antenna's feeding port

3.2 Integrating reconfigurability feature

To enable frequency reconfigurability, the antenna design was augmented with VD modelled as a series RC network. The diode's resistance was fixed at R_s of 1.5Ω , while its capacitance C_v was tuned from 0.01 pF to 1.0 pF. The biasing circuit of the VD, illustrated in Fig. 3(a), designed to control its capacitance variation while ensuring stable operation. It typically includes a series resistance to limit the current flowing through the diode, protecting it from potential damage. Two radio frequency (RF) choke coils are incorporated to mitigate RF currents from passing through the biasing circuit, ensuring that the RF signal remains isolated from the DC supply. A variable DC power supply is used to apply the required reverse bias voltage, enabling precise control over the diode's capacitance. This configuration

allows the VD to achieve the desired capacitance variation, which is essential for tuning and reconfigurability in RF and microwave applications. The diode is modelled as depicted in Fig. 3(b), which includes the parasitic package series inductance L_s , the parallel package capacitance C_p , the VD itself, and its series resistance R_s . The technical specifications of the diodes used in the modelling and prototype implementation, along with their capacitance-voltage (C - V) characteristics, are detailed in reference [25].

As displayed in Fig. 3(c), this configuration induces a continuous frequency shift of ~ 2 GHz within the 24 GHz band, demonstrating the antenna's ability to dynamically adjust its operational frequency in response to varying communication protocols or environmental constraints. Figure 3(d) illustrates the gain-frequency

relationship across the VD capacitance range. The 8-element array achieves a peak gain of 15.8 dB, with minimal degradation (<1 dB) over the majority of the tunable bandwidth. This stability confirms that the reconfigurability mechanism – enabled by the VD capacitance modulation – preserves radiation efficiency while attaining frequency agility. Controlled variations

of the gain ($< \pm 0.5$ dB) across the tuning range further validate the design's robustness, ensuring reliable performance in adaptive scenarios such as interference avoidance or multi-standard operation. These results underscore the viability of VD-based reconfiguration in high-gain antenna arrays, balancing spectral flexibility with consistent radiative performance.

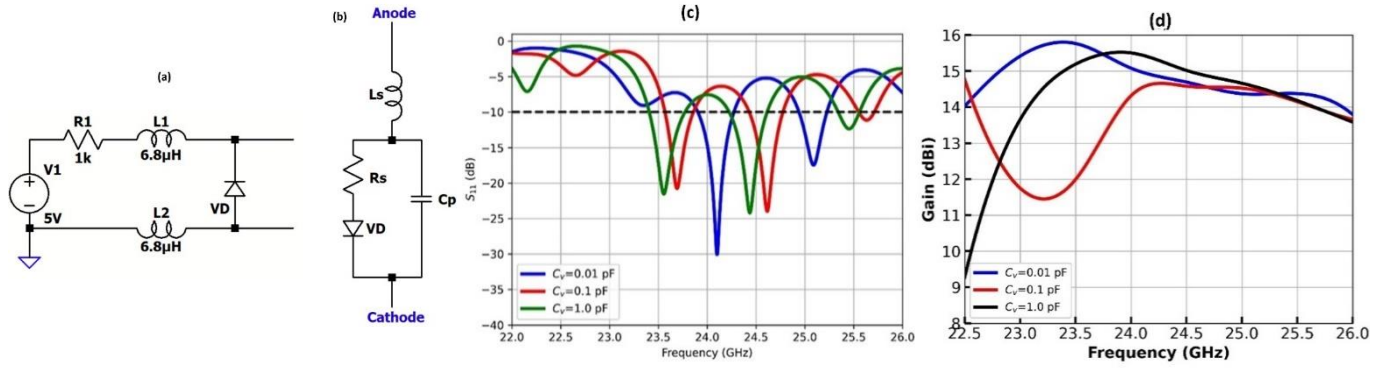


Fig. 3. VD (a) biasing circuit, (b) equivalent circuit model, (c) S_{11} , and (d) gain spectra computed for various values of C_v

Figure 4 illustrates the simulated radiation patterns (RP) of the array in the direction of angle $\phi=0^\circ$ (E-plane) and $\phi=0^\circ$ (H-plane). In the E-plane, the pattern exhibits symmetry about the boresight (0°), with a 14.8 dBi peak gain with HPBW of 74° , enabling broad angular coverage. Conversely, the H-plane pattern demonstrates a narrower HPBW of 11° and a slight 4° angular shift in the main lobe direction, while maintaining the same peak gain of 14.8 dBi. The design achieves a SLL suppression of -24 dB in both planes, underscoring its ability to

minimize off-axis interference. These results highlight the array's capacity to generate highly directional RP with tailored HPBW and suppressed sidelobes, critical for applications demanding precise spatial coverage such as point-to-point communications, radar systems, or interference-sensitive environments. The E-plane symmetry and the controlled H-plane beam shift further validate the efficacy of the Dolph-Chebyshev synthesis method in balancing directivity and pattern integrity.

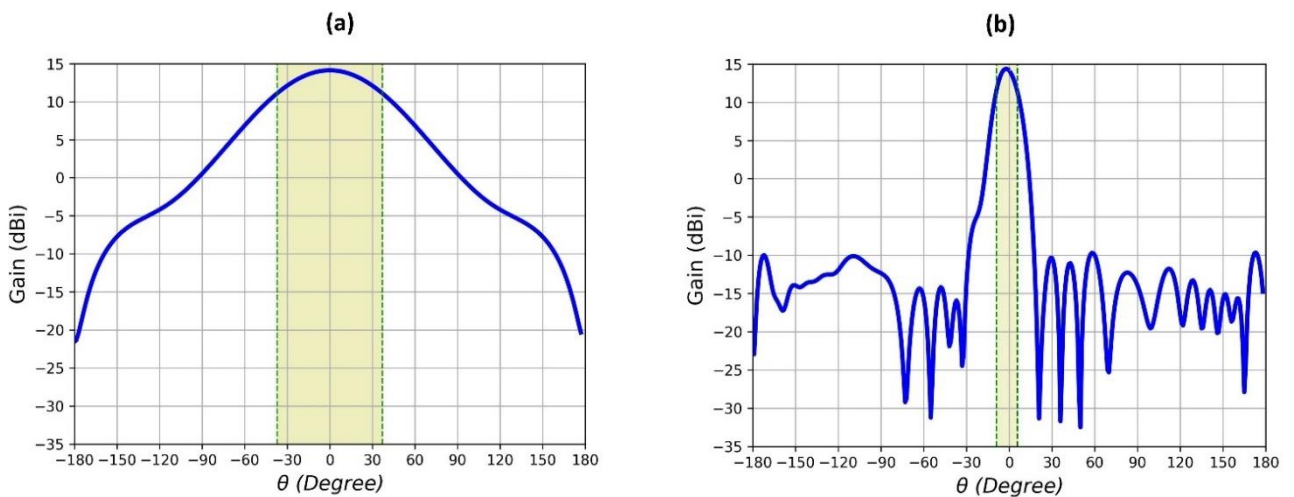


Fig. 4. Simulated radiation patterns of (a) E-plane, (b) H-plane, and (c) 3D patterns

3.3 Intergrading MTM-based decoupling structure

Metamaterials – artificially engineered materials with sub-wavelength structures and unconventional electromagnetic (EM) properties – have emerged as transformative tools in MIMO antenna design. When positioned between radiating elements, MTMs achieve dual objectives: enhancing gain through focused EM energy distribution and improving isolation by absorbing or redirecting unwanted signals. By tailoring

their capacitance and inductance, MTMs reduce coupling between adjacent antennas, ensuring signal integrity and system reliability. These materials leverage their unique permittivity ϵ , permeability μ , and refractive index n to manipulate EM waves in ways unattainable with conventional materials. For instance, negative permittivity and permeability enable anomalous wave propagation, while a negative refractive index permits unprecedented control over light bending, facilitating advanced optical and antenna applications.

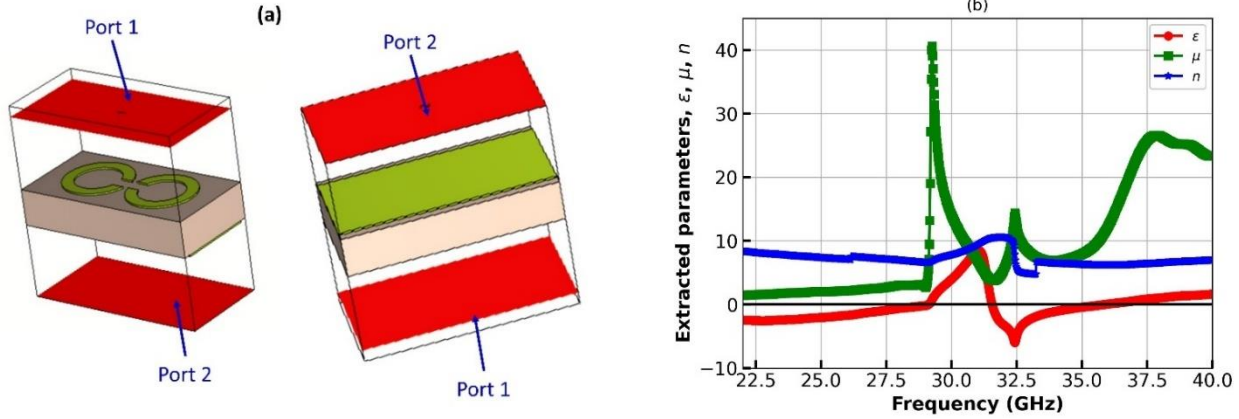


Fig. 5. (a) Top and bottom views of MTM unit cell, and (b) extracted cell parameters ϵ , μ , and n

One key property is permittivity ϵ , which describes material's ability to store electrical energy within an electric field. MTMs allow for precise control over permittivity, including the achievement of negative values, which opens up possibilities for novel EM wave manipulation. Another critical property is permeability μ , which governs material's capacity to sustain internal magnetic fields. By engineering both permeability and permittivity, MTMs can exhibit extraordinary phenomena such as negative refraction and cloaking. Additionally, the refractive index n , which determines how electromagnetic waves propagate through the material, can be tailored in MTMs to achieve negative values. This enables reverse-phase wavefront bending, leading to applications like superlenses and compact waveguides. Together, these properties make MTMs a powerful tool for controlling and innovating electromagnetic wave behavior.

As illustrated in Fig. 5, a proposed MTM unit cell design employs split-ring resonators to reflect interfering signals, effectively acting as a bandstop filter within the MIMO framework. This configuration demonstrates resonant behavior at higher frequencies and achieves targeted negative permittivity within the operational band, significantly suppressing mutual coupling.

3.4 4-port MIMO antenna

The incorporation of MTMs into multiport MIMO configurations offers a transformative approach to mitigating inter-element coupling. By strategically altering surface current distributions on antenna elements, MTMs disrupt the propagation of surface waves – a primary contributor to mutual coupling. This is achieved through the engineered modification of the effective permittivity ϵ and permeability μ in the surrounding medium, which redirects and absorbs EM waves. Such tailored control over EM propagation minimizes undesired interactions between closely spaced antennas, ensuring enhanced isolation and system efficiency.

3.4.1 Radiation pattern analysis

As illustrated in Fig. 6, the 3D radiation patterns provide a comprehensive assessment of the antenna's spatial energy distribution across azimuth, elevation, E-plane, and H-plane orientations. These patterns elucidate critical radiation characteristics, including directivity, 3 dB beamwidth, polarization purity, and gain uniformity. Systematic analysis of these metrics enables precise evaluation of the antenna's directional coverage and signal strength, essential for optimizing performance in real-world deployment scenarios.

3.4.2 Performance enhancement in 4-port MIMO configuration

As illustrated in Fig. 7(a), current excitation at Port 1 induces minimal coupling to Port 2, with the MTM spacer absorbing a significant proportion of surface currents. This attenuation further reduces residual coupling to Ports 3 and 4, demonstrating the spacer's localized decoupling efficacy. Conversely, excitation at Port 2 (Fig. 7b) exhibits stronger coupling to Ports 1 and 3, though its effect on Port 4 remains subdued due to the spacer's targeted current absorption. A symmetrical coupling pattern is observed in Ports 1 and 4 (Fig. 7 c-d), reaffirming the MTM spacer's role in asymmetrically redistributing surface currents. These findings underscore the spacer's capacity to modulate coupling dynamics across the MIMO array, balancing isolation and EM interaction.

The incorporation of MTM-based decoupling structures between MIMO elements resulted in significant performance enhancements across several key metrics. Firstly, gain enhancement was observed, with each antenna array achieving a peak gain of 16 dBi, marking a 1.1 dBi improvement compared to baseline configurations. Secondly, SLL was effectively maintained at -24 dB, ensuring the integrity of the radiation pattern. Thirdly, isolation optimization was achieved, with mutual coupling reduced to a minimum of -60 dB (as illustrated in Fig. 8), while inter-element isolation improved to 38 dB, representing a 17 dB enhancement over the initial design. Lastly, bandwidth expansion was realized, with the operational bandwidth increasing

by 41%, from 390 to 550 MHz. These improvements highlight the effectiveness of MTM-based decoupling structures in enhancing MIMO system performance. These advancements are attributed to the MTM's ability to suppress surface wave propagation by reshaping current flow. The results underscore the dual role of MTMs in simultaneously enhancing gain, bandwidth, and isolation – a critical achievement for high-density MIMO systems operating in interference-prone environments.

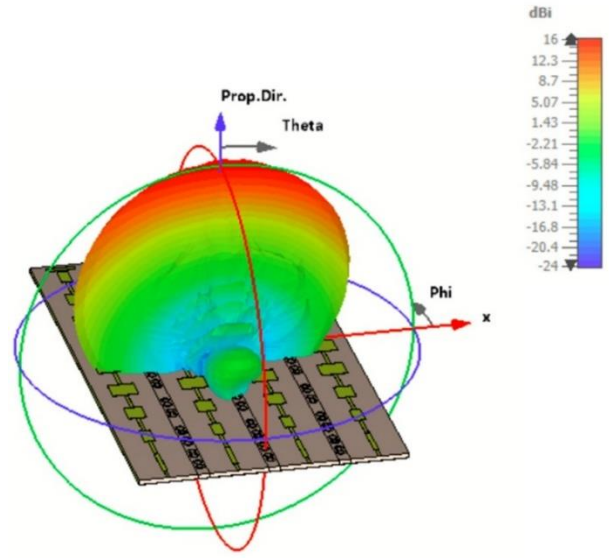


Fig. 6. 3D radiation patterns of 4-port MIMO antenna with MTM spacer

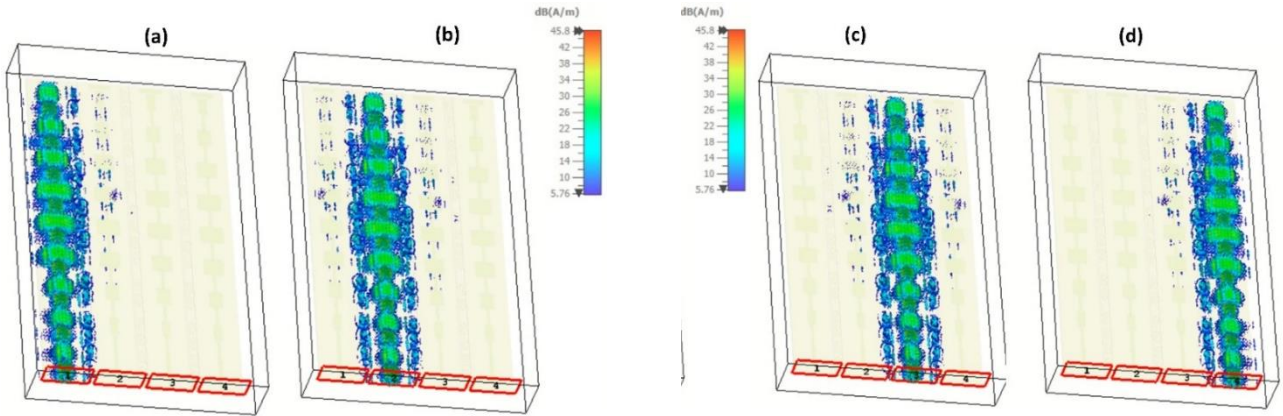


Fig. 7. Surface current distribution of the MIMO antenna excited from (a) port 1, (b) port 2, (c) port 3, and (d) port 4

3.4.3 *S*-parameters validation and isolation performance

The coupling behavior is quantitatively corroborated by the *S*-parameters shown in Fig. 8, which detail the reflection S_{ii} and transmission coefficients S_{ij} of the system. Particularly, the weakest inter-port isolation across the four-element MIMO configuration measures 38.4 dB at resonance, exceeding industry benchmarks for high-performance systems. This stringent isolation aligns with the MTM spacer's ability to suppress mutual coupling while maintaining impedance matching, as evidenced by reflection coefficients below -10 dB across the operational band. Such performance metrics validate the MTM design's dual functionality: mitigating near-field interference and preserving signal integrity at the target frequency of 24 GHz.

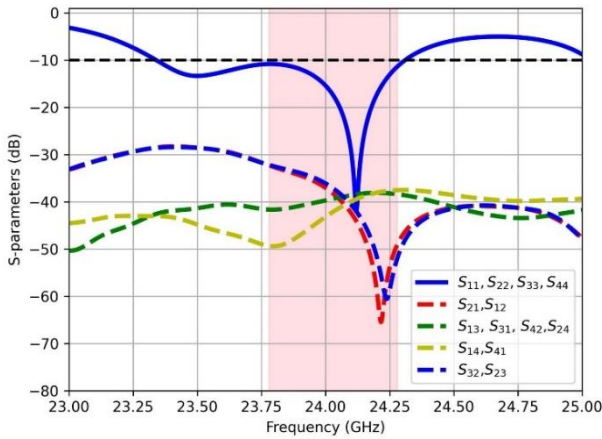


Fig. 8. Simulated *S*-parameters variations versus frequency of 4-port MIMO antenna with metamaterial decoupling structure

The synergy between current redistribution (Fig. 7) and isolation enhancement (Fig. 8) highlights the MTM spacer's critical role in decoupling densely packed

antenna elements. By strategically absorbing surface currents and redirecting EM energy, the spacer achieves a 17 dB improvement in isolation over baseline configurations (as referenced in prior analyses). This advancement not only meets but surpasses the 40 dB threshold required for next-generation wireless systems, positioning the design as a robust solution for interference-limited environments.

Figure 9(a) presents the ECC, and (b) depicts the DG as functions of frequency for the 4-port MIMO antenna. These metrics collectively validate the system's ability to balance low signal correlation with high diversity performance across the operational bandwidth. At the target frequency of 24 GHz, the ECC measures <0.0004 , well below the industry-standard threshold for high-performance MIMO systems. This minimal correlation underscores the antenna's capacity to maintain independent signal paths, a critical requirement for mitigating multipath interference in dense wireless environments. DG peaks very close to 10 dB, aligning closely with theoretical maxima for practical diversity schemes. This result highlights the antenna's ability to exploit spatial and polarization diversity, ensuring robust signal recovery and enhanced link reliability within the designated bandwidth. The observed synergy between low ECC and high DG at 24 GHz directly correlates with the integration of diversity-enhancing modifications, such as orthogonal element placement and MTM-based decoupling. These design choices not only suppress mutual coupling but also optimize channel orthogonality, enabling the antenna to achieve near-ideal MIMO performance. Such metrics affirm the system's suitability for advanced wireless applications, including 5G mmWave networks and high-density IoT deployments, where signal integrity and spectral efficiency are paramount.

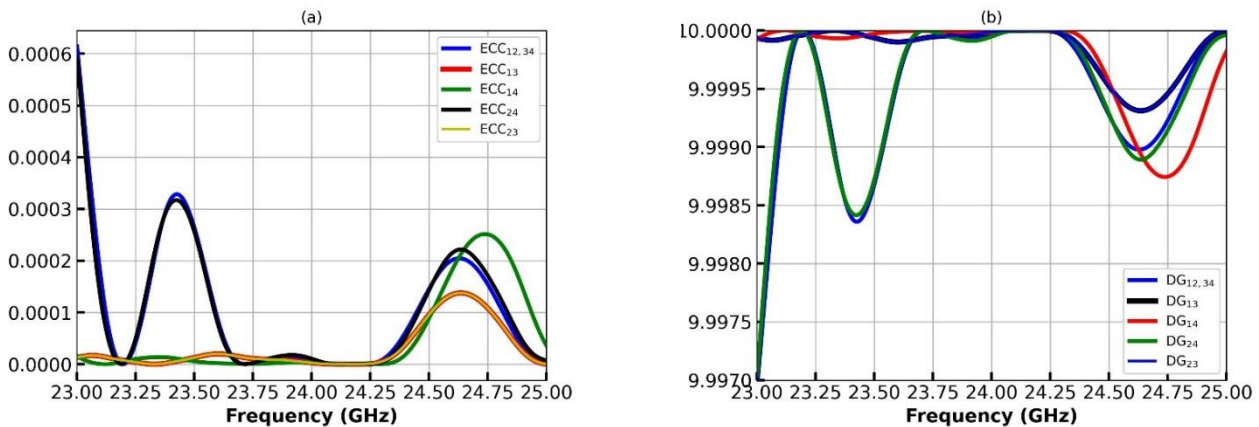


Fig. 9. (a) ECC and (b) DG versus frequency for 4-port MIMO antenna

The computed CCL for the proposed system registered values <0.4 bits/sec/Hz, significantly below the practical threshold for high-performance MIMO configurations. This result corroborates the antenna's ability to minimize inter-channel interference while maximizing spectral efficiency – a critical attribute for high-throughput communication systems. The low CCL, coupled with the previously reported ECC (<0.0004) and DG (~ 10 dB), underscores the design's robustness in maintaining signal integrity, reducing latency, and optimizing data rates across the operational bandwidth.

3.5 Experimental measurement

To measure the S -parameters, including reflection coefficients and mutual coupling among the MIMO ports, an experimental setup was established using essential equipment such as the antenna under test (AUT), a vector network analyzer (VNA), high-quality coaxial cables and RF connectors, and an anechoic chamber. The MIMO antenna is securely mounted, and each port is connected to the VNA using calibrated cables to ensure accurate measurements. The system was calibrated using standard calibration techniques (e.g., short, open, load, and thru) to remove systematic errors and account for cable losses and mismatches. The VNA was configured to measure the S -parameters, where the reflection coefficient (e.g., S_{11} , S_{22}) was obtained by measuring the signal reflected at each port, and mutual coupling (e.g., S_{21} , S_{12}) was determined by measuring the signal transmitted between different ports. Measurements were performed across the desired frequency

range, and data was recorded for each port combination. Postprocessing involves analyzing the S -parameters to evaluate the antenna's performance, including impedance matching, isolation between ports, and mutual coupling levels. Precautions include ensuring proper connections, minimizing cable movement, and performing regular system calibration. The measured results are compared with simulations to validate the MIMO antenna design, providing critical insights into its performance for applications requiring high isolation and low mutual coupling.

Figure 10 provides a comprehensive overview of the reconfigurable antenna design and its experimental evaluation. Figure 10 (a) illustrates the design of a single-array antenna integrated with a VD and its corresponding biasing circuit. The VD enables frequency reconfigurability, allowing the antenna to operate across multiple frequency bands by adjusting the applied bias voltage. Figure 10 (b) shows the prototype of the 4-port MIMO structure. Figure 10 (c) depicts the experimental setup for measuring the S_{11} spectrum, which represents the reflection coefficient. The setup typically includes a vector network analyzer (VNA), coaxial cables, and the AUT, ensuring accurate characterization of the antenna's return loss across the desired frequency range. Figure 10 (d) shows the configuration for measuring the S_{21} parameter, which indicates the transmission coefficient or coupling between antenna ports. This measurement is essential for evaluating the isolation performance of the MIMO structure, particularly in multi-antenna systems where low coupling is crucial for optimal functionality.

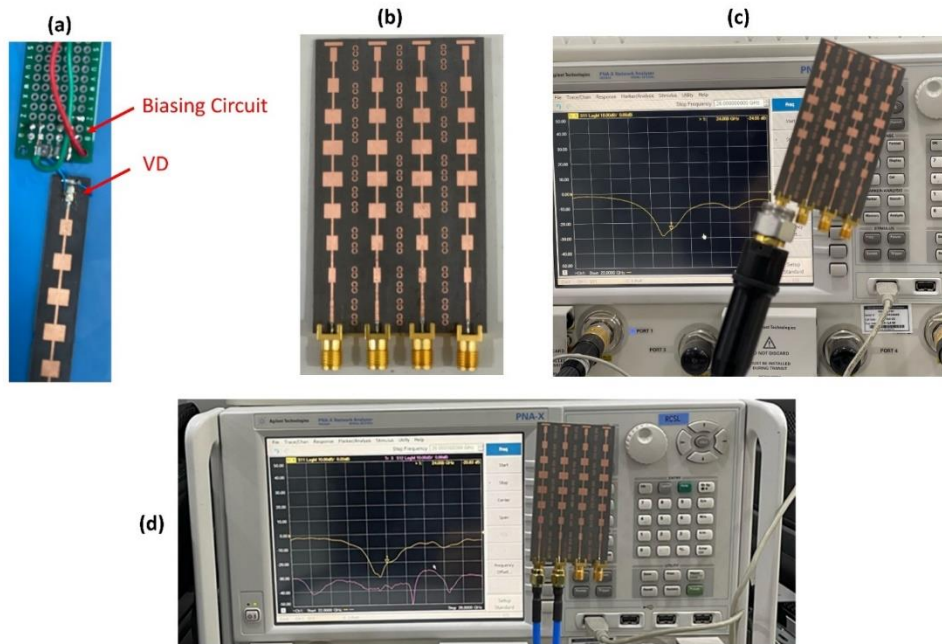


Fig. 10. (a) Reconfigurable single-array antenna incorporating a VD and its associated biasing circuit, (b) prototype of the 4-port MIMO structure, (c) experimental setup for measuring the S_{11} spectrum, and (d) experimental setup for measuring the S_{21} spectrum

Figure 11 presents a comparison between the simulated and measured S_{11} parameter spectra single array antenna. The S_{11} measurement indicates how well the antenna is matched to its input impedance, with lower values representing better impedance matching and reduced signal reflection. The figure highlights a significant bandwidth improvement, extending up to 900 MHz, in the measured S_{11} spectra compared to the simulated results. Additionally, a slight frequency shift of a few megahertz is observed between the simulated and measured data. This shift is a common occurrence in practical measurements and can be attributed to non-idealities in environmental conditions, such as temperature variations, cable losses, and imperfections in the fabrication process. These factors can subtly influence the antenna's performance, leading to minor deviations from the simulated predictions. Despite this shift, the overall agreement between the simulated and measured results remains strong, validating the design's effective-

ness and the accuracy of the simulation model. Similar behavior was observed for the 4-port MIMO structure as shown in Fig. 12.

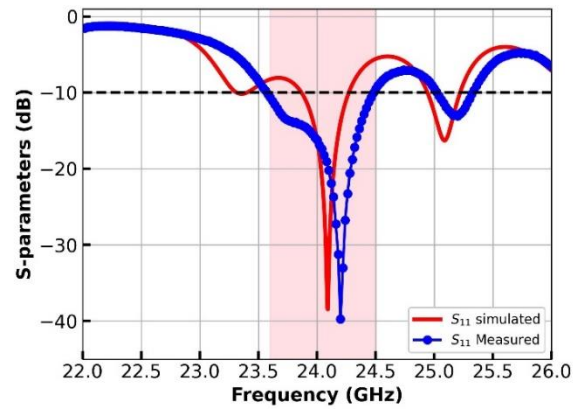


Fig. 11. Comparison of simulated and measured S_{11} parameter spectra of single array antenna

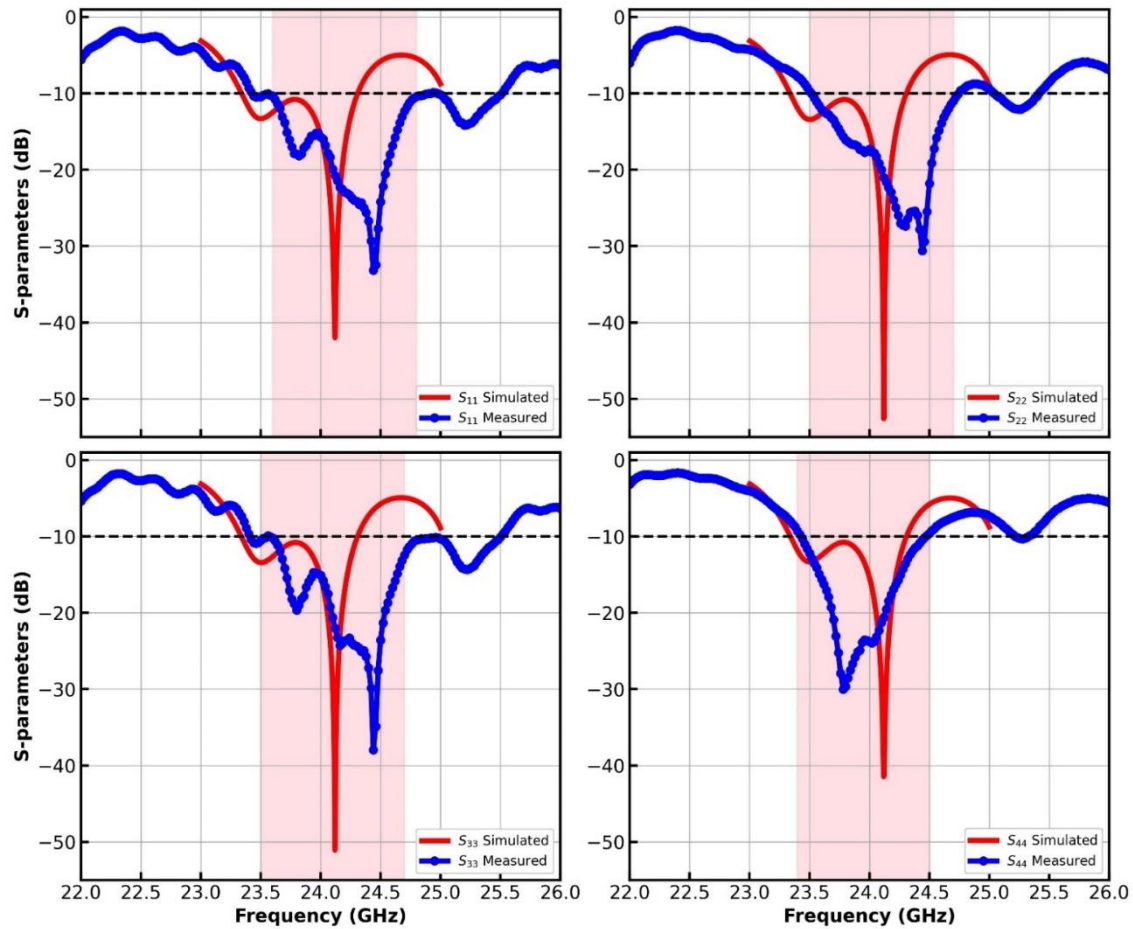


Fig. 12. Simulated and measured S_{11} , S_{22} , S_{33} , and S_{44} spectra of 4-port MIMO antenna with MTM decoupling structure

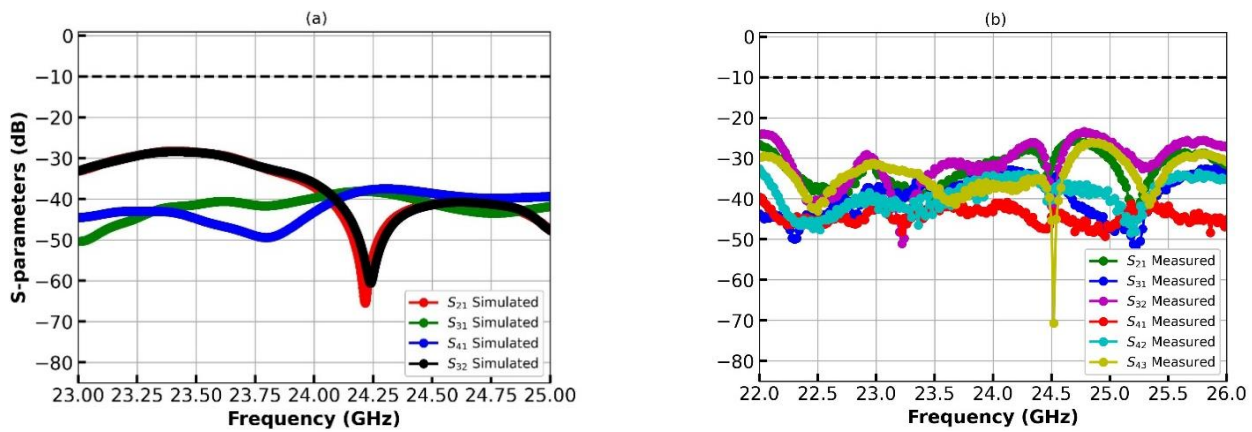


Fig. 13. (a) Simulated, and (b) measured S -parameters spectra of 4-port MIMO antenna with metamaterial decoupling structure

Figure 13 illustrates the isolation performance of the 4-port MIMO antenna integrated with an MTM decoupling structure, focusing on the S_{21} parameter spectra, representing the transmission coefficient between two ports, and indicating the level of isolation achieved between them. Lower S_{21} values correspond to better isolation, which is critical for minimizing mutual coupling and ensuring efficient MIMO operation. The results validate the practical performance of the antenna and confirm the high isolation achieved between the ports, as anticipated by the simulations. Any minor discrepancies, such as slight frequency shifts or variations in isolation levels, can be attributed to fabrication tolerances, environmental factors, or measurement setup non-idealities. At 24 GHz, the measured isolation between the MIMO ports was observed to be in the range of 30 to 50 dB, while the simulated isolation ranged from 38.4 to 45 dB. This close agreement between the measured and simulated results validates the effectiveness of the MTM decoupling structure in achieving high isolation between the antenna ports. The slight variation in the measured isolation, compared to the simulated values, can be attributed to practical factors such as fabrication tolerances, environmental conditions, and measurement setup non-idealities. Despite these minor discrepancies, the results demonstrate excellent isolation performance, which is critical for minimizing mutual coupling and ensuring efficient MIMO operation at the targeted band.

To measure the radiation pattern of an array antenna in azimuth and elevation angles, an experimental setup is established using key equipment such as the AUT, a rotating positioner for azimuth and elevation rotation, a reference antenna (e.g., horn antenna), a VNA, and an anechoic chamber, as shown in Fig. 14. The AUT is mounted on the positioner, aligned at the center of rotation, and placed in the far-field region of the reference antenna, ensuring the far-field distance condition ($R \geq 2D^2/\lambda$) is met. The system is calibrated to account for cable losses and mismatches, and background noise levels are measured. For azimuth pattern measurement, the AUT is rotated in the horizontal plane at small angular steps while recording signal strength and phase at each angle; the same process is repeated for elevation pattern measurement by rotating the AUT in the vertical plane. Data are collected using automated software, and post-processing involves plotting the radiation patterns on polar or Cartesian graphs, normalizing the data, and characterizing the antenna by determining parameters such as HPBW, SLL, null positions, directivity, and gain. Precautions include ensuring proper alignment, minimizing cable movement, and performing regular system calibration. The measured results are compared with simulations to validate the antenna design, providing critical insights into its performance for practical applications.

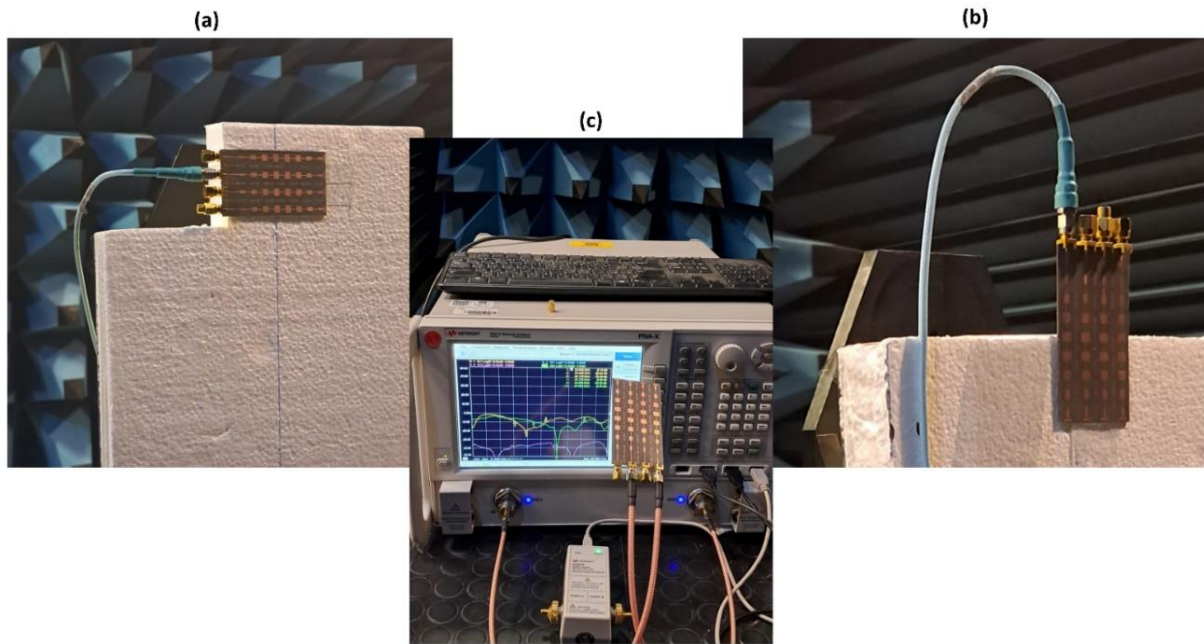


Fig. 14. Experimental setup for radiation pattern measurements of 4-port MIMO antenna in: (a) E-plane, (b) H-plane, (c) measurement of S -parameters

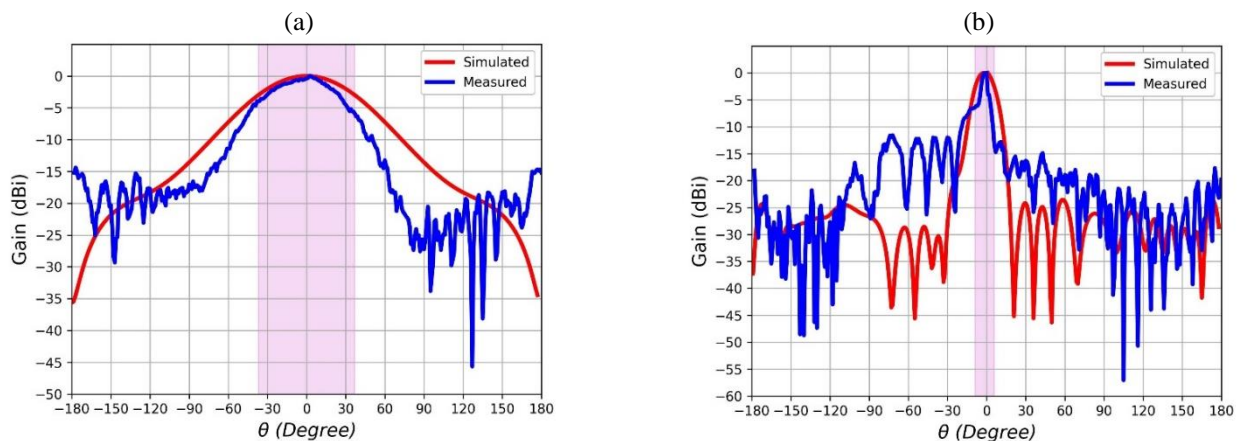


Fig. 15. Simulated and measured radiation pattern of single-array antenna evaluated in (a) E-plane, and (b) H-plane. The gain was normalized to the maximum gain at $\theta = 0^\circ$.

For the E-plane RP depicted in Fig. 15(a), a high degree of agreement is observed between the simulated results and the experimental measurements, particularly at lower angles. This close alignment at lower angles indicates that the antenna design and simulation accurately predict the main lobe characteristics and near-angle side lobe behavior. However, at higher angles, the measured SLL is slightly elevated compared to the simulation results. This discrepancy can be attributed to the influence of the measurement environment. In a non-ideal environment, factors such as reflections from surrounding objects, multipath interference, and external electromagnetic noise can distort the radiation pattern, particularly at higher angles where the antenna's

sensitivity to environmental effects is more pronounced. These environmental influences are not accounted for in the simulation, which assumes an ideal, reflection-free environment. Despite this, the overall consistency between the simulation and measurement at lower angles validates the design, while the minor deviations at higher angles highlight the importance of conducting measurements in a more controlled environment. A similar behavior was also confirmed in the H-plane measurements, as illustrated in Fig. 16 (b). The results demonstrate excellent agreement between the simulated and measured radiation patterns at lower angles, further validating the accuracy of the antenna design and simulation model in predicting the main lobe characteristics. However, at

higher angles, a slight increase in the SLL is observed in the experimental measurements compared to the simulation results. This deviation can again be attributed to the effects of the measurement environment.

Figure 16 depicts similar results obtained for the MIMO structure when measured in both the E-plane and

H-plane, with specific evaluations conducted for Port 1 and Port 3. The symmetrical design of the antenna ensured consistent performance across all ports, with only minor variations observed due to coupling effects between adjacent elements. These measurements confirm the stability and reliability of the antenna's radiation characteristics across the operational frequency band.

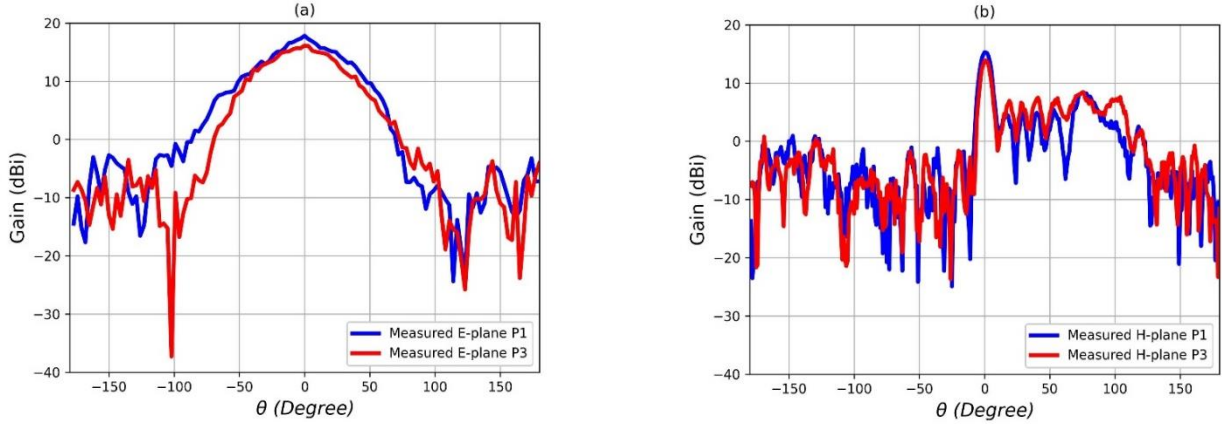


Fig. 16. Measured radiation pattern of 4-port MIMO antenna (ports 1 and 3) evaluated in (a) E- and (b) H-planes

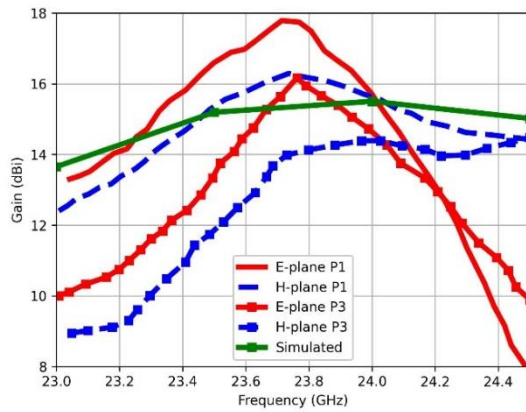


Fig. 17. Measured and simulated gain of 4-port MIMO antenna (ports 1 and 3) evaluated in (a) E-plane, and (b) H-plane

Figure 17 illustrates the measured gain versus frequency for the 4-port MIMO antenna, evaluated practically for Port 1 and Port 3. For the remaining ports (Port 2 and Port 4), similar results were obtained due to the symmetrical design of the antenna structure. In this plot, the peak gain reaches a maximum of 17.8 dBi for the E-plane of Port 1, while the minimum gain observed is 14 dBi for the H-plane of Port 3. The slight reduction

in gain for Port 3, observed in both the E-plane and H-plane, can likely be attributed to destructive interference. This interference occurs because Port 3 is more significantly affected by the coupling and interaction with neighboring antenna elements compared to Port 1. Despite this, the results demonstrate a stable gain variation across both the E-plane and H-plane within the frequency band of interest, confirming the antenna's robust performance for MIMO applications.

The comparison, listed in Tab. 2, highlights performance of various designs reported in the literatures. The proposed design achieves a bandwidth of 0.9 GHz, a peak gain of 17.8 dBi, an excellent measured SLL of -21 dB (in the E-plane), and high port isolation of 38.4 dB, outperforming most references in many aspects. Although its bandwidth is narrower than some designs like [27] and [29], it remains suitable for targeted applications, and its compact size enhances practicality for integration. The combination of high gain, low SLL, and strong isolation demonstrates superior interference management and signal clarity, making the proposed antenna a competitive and versatile solution for advanced communication and radar systems.

Table 2. Performance comparison of this work with other studies based on various evaluation metrics

Reference No.	Recon-figurability?	Operating frequency (GHz)	Number of MIMO ports	Array elements	Dimensions (mm ³)	Substrate	Bandwidth (GHz)	Gain (dBi)	SLL (dB)	Isolation (dB)
[12]	No	24.0	2	2×2	58×55×0.254	Rogers 4350B	0.510	5.2	NA	36.7
[27]	No	24.5	1	8×8	40×6×0.787	Rogers 4350	2.0	20.6	−20	NA
[28]	No	24.0	2	2×2	36×22×0.254	Rogers 4350B	1.0	12.5	−15	34
[29]	No	24.0	2	2×2	40×06×0.254	RT-Duroid 5880	4.44	9.8	NA	45
[30]	No	24.0	6	1×7	105.5×56.6×0.25	RT-Duroid 5880	0.150	13.7	−11	17
This work	Yes	24.131	4	1×8	10×80×0.787	RT-Duroid 5880	0.9	17.8	−21 (E-plane) −11 (H-plane)	38.4

4 Conclusion

A four-port frequency-reconfigurable MIMO antenna, optimized for high gain, minimal mutual coupling, and suppressed SLL, has been meticulously engineered to address the stringent demands of ISM24GHz band sensing and automotive radar systems. The design integrates 1×8 microstrip patch arrays, a MTM absorber with a SRR configuration, and a VD for dynamic frequency tuning. Through rigorous electromagnetic simulations and parametric optimization, the antenna achieves 17.8 dBi peak gain, inter-port isolation exceeding 38.4 dB at 24.125 GHz, and an SLL suppressed to −21 dB, ensuring robust performance in interference-prone environments. Key performance metrics include a HPBW of 74° in the E-plane and 11° in the H-plane at 24.120 GHz, offering a balance between broad azimuthal coverage and directional precision. The antenna achieves an impedance bandwidth of 900 MHz, complies with global 24 GHz ISM band regulations, and ensures robust MIMO operation with inter-port isolation ≥ 38.4 dB, an ECC < 0.0004 , and DG ≈ 10 dB. A decoupling strategy SRR-based MTM absorber reduces mutual coupling by 17 dB by disrupting surface wave propagation, acting as a bandstop filter to enhance gain and isolation. Compared to state-of-the-art designs, the antenna excels in gain, isolation, and bandwidth flexibility, making it ideal for next-generation automotive radars, mmWave sensing, and high-density IoT networks, where spectral efficiency, interference resilience, and compact design are critical.

Acknowledgments

The authors gratefully acknowledge Qassim University (QU), represented by the Deanship of Graduate Studies and Scientific Research for the financial support of this project during the academic year 1446 AH/2025 AD (Geel Baheth-1446/2025).

The authors also acknowledge Prince Sultan Defense Studies and Research Center (PSDSRC) and King Abdulaziz City for Science and Technology (KACST) for fabricating and measuring the antenna reported in this project.

References

- [1] C. Waldschmidt, J. Hasch, and W. Menzel, "Automotive radar – From first efforts to future systems," *IEEE Journal of Microwaves*, vol. 1, no. 1, pp. 135–148, 2021. DOI: <https://doi.org/10.1109/JMW.2020.3033616>
- [2] V. Issakov, Microwave circuits for 24 GHz automotive radar in silicon-based technologies. *Springer Science & Business Media*, 2010. DOI: <https://doi.org/10.1007/978-3-642-13598-9>
- [3] T. Arai, T. Usugi, T. Murakami, S. Kishimoto, Y. Utogawa, M. Kohtani, I. Ando, K. Matsunaga, C. Arai, and S. Yamaura, "A 77-GHz 8RX3TX transceiver for 250-m long-range automotive radar in 40-nm CMOS technology," *IEEE Journal of Solid-State Circuits*, vol. 56, no. 5, pp. 1332–1344, 2021. DOI: [10.1109/JSSC.2021.3050306](https://doi.org/10.1109/JSSC.2021.3050306)
- [4] J. Hasch, E. Topak, R. Schnabel, T. Zwick, R. Weigel, and C. Waldschmidt, "Millimeter-wave technology for automotive radar sensors in the 77 GHz frequency band," *IEEE Transactions on Microwave Theory and Techniques*, vol. 60, no. 3, pp. 845–860, 2012. DOI: [10.1109/TMTT.2011.2178427](https://doi.org/10.1109/TMTT.2011.2178427)
- [5] M. Schneider, "Automotive radar-status and trends," in *German Microwave Conference*, 2005, pp. 144–147.
- [6] K. Ohguchi, M. Shono, and M. Kishida, "79 GHz band ultra-wideband automotive radar," *Fujitsu Ten Tech. J.*, vol. 39, pp. 9–14, 2013.
- [7] N. Kathuria and B. C. Seet, "24 GHz flexible antenna for Doppler radar-based human vital signs monitoring," *Sensors*, vol. 21, no. 11, p. 3737, 2021. DOI: <https://doi.org/10.3390/s21113737>
- [8] S. Park, S. Kim, D. K. Kim, J. Choi, and K. Y. Jung, "Numerical study on the feasibility of a 24 GHz ISM-band Doppler radar antenna for near-field sensing of human respiration in electromagnetic aspects," *Applied Sciences*, vol. 10, no. 18, p. 6159, 2020. DOI: <https://doi.org/10.3390/app10186159>
- [9] Y. S. Won, C. H. Kim, and S. G. Lee, "Range resolution improvement of a 24 GHz ISM band pulse radar—A feasibility study," *IEEE Sensors Journal*, vol. 15, no. 12, pp. 7142–7149, 2015. DOI: [10.1109/JSEN.2015.2469154](https://doi.org/10.1109/JSEN.2015.2469154)

- [10] F. Alimenti, V. Palazzi, C. Mariotti, M. Virili, G. Orecchini, S. Bonafoni, L. Roselli, and P. Mezzanotte, "A 24-GHz front-end integrated on a multilayer cellulose-based substrate for Doppler radar sensors," *Sensors*, vol. 17, no. 9, p. 2090, 2017. <https://doi.org/10.3390/s17092090>
- [11] H. L. Lee, W. G. Lim, K. S. Oh, and J. W. Yu, "24 GHz balanced Doppler radar front-end with Tx leakage canceller for antenna impedance variation and mutual coupling," *IEEE Transactions on Antennas and Propagation*, vol. 59, no. 12, pp. 4497–4504, 2011. DOI: 10.1109/TAP.2011.2165486
- [12] S. Kim, D. K. Kim, Y. Kim, J. Choi, and K. Y. Jung, "A 24 GHz ISM-band Doppler radar antenna with high isolation characteristics for moving target sensing applications," *IEEE Antennas and Wireless Propagation Letters*, vol. 18, no. 7, pp. 1532–1536, 2019. DOI: 10.1109/LAWP.2019.2922008
- [13] L. C. Chang, Y. H. Lin, S. Y. Chen, H. T. Chou, and H. Wang, "A duplexing hybrid slot antenna design with high isolation for short-range radar detection and identification applications at 24 GHz band," *IEEE Transactions on Antennas and Propagation*, vol. 70, no. 4, pp. 2468–2479, 2021. DOI: 10.1109/TAP.2021.3118713
- [14] S. Hamdan, E. K. Hamad, H. A. Mohamed, and S. A. Khaleel, "High-performance MTM inspired two-port MIMO antenna structure for 5G/IoT applications," *Journal of Electrical Engineering*, vol. 75, no. 3, pp. 214–223, 2024. DOI: <https://doi.org/10.2478/jee-2024-0026>
- [15] J. Hasch, E. Topak, R. Schnabel, T. Zwick, R. Weigel, and C. Waldschmidt, "Millimeter-wave technology for automotive radar sensors in the 77 GHz frequency band," *IEEE Transactions on Microwave Theory and Techniques*, vol. 60, no. 3, pp. 845–860, 2012. DOI: 10.1109/TMTT.2011.2178427
- [16] L. Daniel and M. Gashinova, "Sub-THz radar imagery for automotive application," in *2022 19th European Radar Conference (EuRAD)*, 2022, pp. 261–264. DOI: 10.23919/EuRAD54643.2022.9924931
- [17] E. Hyun, Y. S. Jin, and J. H. Lee, "Design and Implementation of 24 GHz Multichannel FMCW Surveillance Radar with a Software-Reconfigurable Baseband," *Journal of Sensors*, vol. 2017, no. 1, p. 3148237, 2017. <https://doi.org/10.1155/2017/3148237>
- [18] M. A. Almasi, H. Mehrpouyan, V. Vakilian, N. Behdad, and H. Jafarkhani, "A new reconfigurable antenna MIMO architecture for mmWave communication," in *2018 IEEE International Conference on Communications (ICC)*, 2018, pp. 1–7. DOI: 10.1109/ICC.2018.8422414
- [19] P. Sharma, R. N. Tiwari, P. Singh, P. Kumar, and B. K. Kanaujia, "MIMO antennas: Design approaches, techniques and applications," *Sensors*, vol. 22, no. 20, p. 7813, 2022. DOI: <https://doi.org/10.3390/s22207813>
- [20] M. Shaban, "Design and Modeling of a Reconfigurable Multiple Input, Multiple Output Antenna for 24 GHz Radar Sensors," *Modelling*, vol. 6, no. 1, p. 2, 2025. DOI: <https://doi.org/10.3390/modelling6010002>
- [21] G. Gennarelli, C. Noviello, G. Ludeno, G. Esposito, F. Soldovieri, and I. Catapano, "24 GHz FMCW MIMO radar for marine target localization: A feasibility study," *IEEE Access*, vol. 10, pp. 68240–68256, 2022. DOI: 10.1109/ACCESS.2022.3186052
- [22] J. Qian, H. Zhu, M. Tang, and J. Mao, "A 24 GHz microstrip comb array antenna with high sidelobe suppression for radar sensor," *IEEE Antennas and Wireless Propagation Letters*, vol. 20, no. 7, pp. 1220–1224, 2021. DOI: 10.1109/LAWP.2021.3075887
- [23] K. Zhi, C. Pan, H. Ren, and K. Wang, "Power scaling law analysis and phase shift optimization of RIS-aided massive MIMO systems with statistical CSI," *IEEE Transactions on Communications*, vol. 70, no. 5, pp. 3558–3574, 2022. DOI: 10.1109/TCOMM.2022.3162580
- [24] C. A. Balanis, *Antenna Theory: Analysis and Design*. John Wiley & Sons, 2005.
- [25] S. J. Orfanidis, *Electromagnetic waves and antennas*. Rutgers University, 2002.
- [26] R. Strohman, Z. Fritts, G. Chensue et al., "Characterization and Modeling of Varactor Diodes for Parametric Circuits," *TechRxiv*, Oct. 07, 2024. DOI: 10.36227/techrxiv.172833691.19029304/v1.
- [27] W. Yang, Y. Yang, W. Che, L. Gu, and X. Li, "A novel 24-GHz series-fed patch antenna array for radar system," in *2016 IEEE International Workshop on Electromagnetics: Applications and Student Innovation Competition (iWEM)*, 2016, pp. 1–4. DOI: 10.1109/iWEM.2016.7505065
- [28] A. Sharma, S. Das, B. K. Kanaujia, D. Gangwar, S. Kumar, S. P. Singh, and A. L. Elsherbeni, "In-band RCS reduction and isolation enhancement of a 24 GHz radar antenna using metamaterial absorber for sensing and automotive radar applications," *IEEE Sensors Journal*, vol. 20, no. 21, pp. 13086–13093, 2020. DOI: 10.1109/JSEN.2020.3002337
- [29] M. Sharma, A. K. Gautam, N. Agrawal, and N. Singh, "Design of MIMO planar antenna at 24 GHz band for radar, communication and sensors applications," *AEU-International Journal of Electronics and Communications*, vol. 136, p. 153747, 2021. DOI: <https://doi.org/10.1016/j.aeue.2021.153747>
- [30] A. Mukherjee and D. Sarkar, "Interleaved MIMO Radar for Marine Target Tracking Application," in *2024 4th URSI Atlantic Radio Science Meeting (AT-RASC)*, 2024, pp. 1–4. DOI: 10.46620/URSIATRASC24/AEEG8350

Received 30 March 2025